

1 **The unique features in the four-day widespread extreme rainfall event over North**
2 **China in July 2023**

3
4 Jinfang Yin^{1,2,3}, Feng Li¹, Mingxin Li¹, Rudi Xia¹, Xinghua Bao¹,
5 Jisong Sun¹, and Xudong Liang¹

6
7 ¹ State Key Laboratory of Severe Weather, Chinese Academy of Meteorological
8 Sciences, Beijing 100081, China

9 ² Research Center for Disastrous Weather over Hengduan Mountains & Low-Latitude
10 Plateau, China Meteorological Administration (CMA), Kunming 650034, China

11 ³ Shigatse National Climatological Observatory, CMA, Shigatse 857000, China

12
13 Submitted to *Natural Hazards and Earth System Sciences (NHES)*

14 August 2024

15 Second round November 2024

16
17 Corresponding author: Jinfang YIN

18 E-mail: yinjf@cma.gov.cn

19 **ABSTRACT**

20 Synoptic forcings have traditionally played a pivotal role in extreme rainfall over North
21 China. However, there are still large unexplained gaps in understanding the formation of
22 extreme rainfalls over this region. The heavy rainfall event, lasting from 29 July to 2 August
23 2023 (referred to as “23·7” event), is characterized by long duration, widespread coverage,
24 and high accumulated rainfall over North China. Overall, the persistent extreme rainfall is
25 closely associated with the remnant vortex originating from typhoon Doksuri (2305), tropical
26 storm Khanun (2306), and the unusual westward extended Western North Pacific Subtropical
27 High (WNPSH), as well as quasi-stationary cold dry air masses surrounding North China on
28 the west and north sides. Based on wind profiles and rainfall characteristics, the life history of
29 the “23·7” event is divided into two stages. In the first stage, the western boundary of the
30 WNPSH was destroyed by the tropical storm Doksuri, appearing that the WNPSH retreated
31 eastward with decreasing height. As a result, an inclined vertical distribution on the western
32 boundary was established below 500 hPa. Therefore, convections were limited by the tilted
33 WNPSH with warm-dry cover embedded in the low-to-middle troposphere. Meanwhile, the
34 orography in the west of North China was controlled by cold air masses above nearly 3.0 km.
35 Combining the orographic and cold air blockings, only a shallow southeasterly layer
36 (between 1.3 and 3.0 km) can overpass mountains. Although the warm and moist
37 southeasterly flows were lifted by orography, no convections were triggered because of the
38 local capped cold and dry air masses overhead. Under this framework, equivalent potential
39 temperature (θ_e) gradients were established between warm humid and dry cold air masses,
40 similar to a warm front, causing warm air to lift and generate widespread rainfall but low
41 intensity. However, the lifting was too weak to allow convection to be highly organized. In the
42 second stage, the WNPSH was further destroyed by enhanced Khanun, and thus the
43 embedded warm-dry cover associated with the tilted WNPSH was significantly thinned.
44 Consequently, convections triggered by orographic blocking can move upward and
45 consequently further develop, forming deep convections. Comparatively speaking, the
46 convections in the second stage are much deeper than those in the first stage. The results
47 gained herein may shed new light on better understanding and forecasting of long-lasting
48 extreme rainfall.

删除的内容: western

带格式的: 字体: Times New Roman

删除的内容: s

删除的内容: h

删除的内容: western Pacific subtropical high (

删除的内容:)

54 **1. Introduction**

55 A persistent severe rainfall event occurred over central and North China during the period
56 from 29 July to 2 August 2023 (referred to as “23·7” event), which was regarded as one of the
57 precipitation extremes of 2023 globally (Fowler et al., 2024). Despite the rainfall in low
58 intensity, it was long-lasting and widespread, resulting in large accumulated rainfall. Overall,
59 the average accumulated rainfall over North China (including Beijing, Tianjin, and Hebei
60 Province) was 175 mm, which was approximately 1/3 of the average annual precipitation in this
61 region. Flooding from this event affected 1.3 million people, bringing severe human casualties
62 and economic losses. The sustained severe rainfall over Beijing left 33 people dead and 18
63 missing persons. One of the distinct features of this rainfall event was closely associated with
64 the remnant vortex originating from typhoon Doksuri (2305), tropical storm Khanun (2306),
65 unusual westward extended Western North Pacific Subtropical High (WNPSH), and
66 quasi-stationary cold dry air masses surrounding North China on their west and north sides.

67 It is common for rainfall occurrence over North China due to strong water vapor supply by
68 tropical cyclones over the East China Sea and/or Southern China Sea (e.g., Ding, 1978; Feng
69 and Cheng, 2002; Yin et al., 2022c). Like the “96·8” severe rainfall event (Sun et al., 2006; Bao
70 et al., 2024), the present persistent rainfall event was closely linked to two tropical storms of
71 Doksuri (2305) and Khanun (2306). Note that the Doksuri weakened to a typhoon remnant
72 vortex (typhoon-low pressure) at this moment as it moved inland after landfalling, while the
73 tropical storm Khanun was in a fast-developing stage. The tropical storm Khanun and the
74 typhoon remnant vortex built jointly a water vapor bridge, transporting a large amount of water
75 vapor to North China from the East China Sea. Previous studies (e.g., Hirata and Kawamura,
76 2014; Gao et al., 2022; Yang et al., 2017) pointed out that large amounts of water vapor brought
77 by a typhoon over the North Pacific were favorable for severe rainfall generation in eastern
78 China.

79 In the last several decades, considerable attention was paid to the remote rainfall events
80 associated with tropical cyclones, with substantial progress made (e.g., Wang et al., 2009; Xu et
81 al., 2023a; Xu et al., 2023b; Lin and Wu, 2021). Commonly, sufficient water vapor provided by a
82 tropical cyclone plays an important role in extreme rainfall over North China (e.g., Rao et al.,

删除的内容:

删除的内容: province

删除的内容: heavy

删除的内容: western

删除的内容: s

删除的内容: h

删除的内容: heavy

删除的内容: and

删除的内容: heavy

删除的内容: and

删除的内容: has been

94 2023; Xu et al.,2023b). Besides, many studies confirmed that the WNPSH is closely related to
95 water vapor transportation and the spatial distribution of rainfall (e.g., Hu et al.,2019; Gao et al.,
96 2022). Additionally, orographic forcing of the approaching warm and moist unstable airflow
97 plays a critical role in determining the location of convection initialization, although sometimes
98 orographic forcing played a small role compared to Typhoon’s circulation (Wang et al.,2009).
99 Moreover, severe rainfall can be generated by the complicated cloud microphysical processes
100 due to the interactions between tropical oceanic warm-moist and mid-latitude cold-dry air
101 masses (Wang et al.,2009; Xu and Li,2017; Xu et al.,2021). Despite some experiences gained,
102 there are still large unexplained gaps in understanding the formation of extreme rainfall (Meng
103 et al.,2019).

删除的内容: heavy

104 Due to the tremendous impacts of the “23·7” event, many scholars have carried out
105 studies of the event from various aspects. Li et al (2024) provided a detailed analysis of fine
106 characteristics of the precipitation using radar and dense rain gauge observations. Xia et al.
107 (2025) investigated extreme hourly rainfalls at different episodes. Fu et al. (2023) paid attention
108 to the effects of dynamic and thermodynamic conditions on precipitation, while Gao et al.
109 (2024) focused on the impact of mountain-plain thermal contrast on precipitation distribution.
110 Although operational forecasts gave a reasonable spatial distribution of precipitation at that
111 time, the precipitation intensity was underestimated significantly. Indeed, it is found that, in
112 this event, the unusual westward-extended WNPSH played an important role in modulating
113 convection initialization and development, with several unusual features revealed. However,
114 given the unusual westward-extended WNPSH, some unexplainable questions have been raised,
115 while little attention has been paid to date. Firstly, what mechanism(s) could account for the
116 persistent severe rainfall? Besides, what is the role of the unusual westward-extended WNPSH
117 in governing the rainfall over North China? Therefore, we are motivated to conduct the present
118 modeling study to answer those questions.

删除的内容: density

删除的内容:

删除的内容: , and

删除的内容: were found

删除的内容: Given

删除的内容: westward

删除的内容: heavy

删除的内容: westward

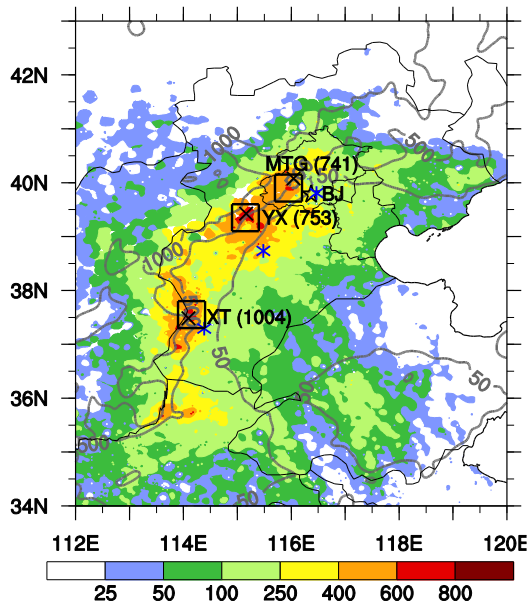
119 The rest of the paper is organized as follows. A detailed description of the main features of
120 extreme rainfall and synoptic-scale weather conditions is documented. Section 3 provides
121 detailed model configuration and verification against observations. We present a detailed
122 analysis of the extreme rainfall production in Section 4. The paper finishes with conclusions

132 and outlooks.

133 2. Properties of rainfall and wind profiles

134 2.1 Characteristics of rainfall

135 Figure 1 shows the spatial distribution of 96-h accumulated rainfall from observations
136 during the period from 0000 UTC 29 July to 0000 UTC 2 August 2023, with the peak amount of
137 1004 mm at Liangjiazhuang station near Xingtai, Hebei Province of North China.
138 Exceptionally long duration of rainfall is a notable feature of the event, with the longest
139 duration being 80 hours within the four days at some stations. The spatial distribution of the rain
140 belt with three severe rainfall cores is consistent with the orography direction of the Yanshan
141 Mountains on the north as well as of the Taihang Mountains on the south, suggesting that
142 orography plays an important role in the precipitation. It should be emphasized that three
143 rainfall cores, marked by Mentougou (MTG, 741 mm) in Beijing, and Yixian (YX, 753 mm)
144 and Xingtai (XT, 1004 mm) in Hebei Province, correspond respectively to the regions with
145 large topographic gradients (Fig. 1). Please refer to Li et al. (2024) for a detailed analysis of fine
146 features of this rainfall event.



147
148 **Fig. 1** Spatial distribution of 96-h accumulated rainfall (mm, shadings) from the intensive
149 surface rain gauge observations during the period from 0000 UTC 29 July to 0000 UTC 2

删除的内容: heavy

删除的内容: and

152 August 2023; Gray contours denote orography from 50 m to 1000 m as marked. Three rainfall
153 cores in Mentougou (MTG) in Beijing, and Yixian (YX) and Xingtai (XT) in Hebei Province
154 are denoted by squares, with the values in parentheses indicating the maximum accumulated
155 rainfall (marked by crisscross sign ×) for the regions, respectively. The blue asterisks (✱)
156 represent the locations of wind profiler observational stations near the three rainfall cores. The
157 start (☆) sign indicates the location of Beijing (BJ) City. (Similarly for the rest of figures).

158 2.2 Wind profiles

159 The observed wind profiles near MTG, YX, and XT are shown in Fig. 2. It is found that
160 temporal variations in horizontal wind fields are distinct during the rainfall event. Taking the
161 wind profiles near MTG as an example (Fig. 2a), the easterly or southeasterly wind at the
162 levels below 4 km was increased gradually from 2 m s⁻¹ at 1200 UTC 28 to 24 m s⁻¹ at 1200
163 UTC 30 July 2023. The easterly or southeasterly wind lasted to 0400 UTC 31 July 2023,
164 turned southerly except for near the ground, and then turned southwesterly near 0400 UTC 1
165 August 2023. After 0400 UTC 31 July, wind speed decreased significantly and then increased
166 drastically. More specifically, the wind speed was decreased from 8 m s⁻¹ to 2 m s⁻¹, and then
167 increased to 14 m s⁻¹ near 1 km above the ground. However, opposite variations were
168 observed above 4 km. One can see that the horizontal wind shifted from southwesterly to
169 southerly, then back to southwesterly. Overall, the shift in wind direction and speed altered the
170 vertical wind shear, which directly affected the development and organization of subsequent
171 convection (Pucik et al., 2021). Similar variations can also be found at YX and XT stations,
172 although the timing of changes is not synchronized with each other (Fig. 2c, d). The variations
173 proceeded from south to north, starting first at XT and finally at MTG, in pace with the typhoon
174 moving from south to north.

删除的内容: marked

删除的内容: and

删除的内容: indicate

删除的内容: Obvious

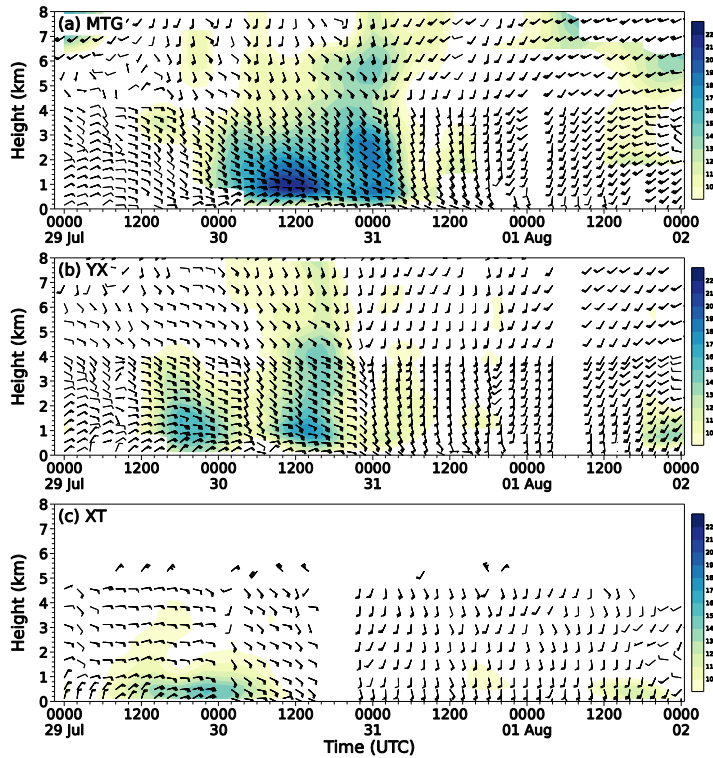
删除的内容: can be seen

删除的内容: gradually

删除的内容: can also be seen

删除的内容: as

删除的内容: moved



184
 185 **Fig. 2** Temporal evolution of the wind profile (a full barb is 4 m s^{-1} , and shadings denote wind
 186 speed over 10 m s^{-1}) from observations near (a) MTG, (b) YX, and (c) XT during the period of
 187 0000 UTC 29 July to 0000 UTC 2 August 2023. Note that only the wind profile below 5 km
 188 above the ground is able to be observed due to the limitation of the instrumentation near
 189 Xingtai (XT). (see Fig. 1 their locations).

190 **2.3 Synoptic conditions on 28 July 2023**

191 Figure 3 displays a weather chart on 500 hPa at 1200 UTC 28 July 2023. One can see that
 192 the large-scale flow patterns exhibited a coexistence of the tropical storm Khanun_(2306) with a
 193 remnant vortex originating from typhoon Doksuri_(2305)*. Note that the Khanun was in the
 194 rapid development stage then, while the vortex weakened significantly at that time. Another
 195 important weather system was the WNPSH (denoted by the 588 isoline) with a square-head

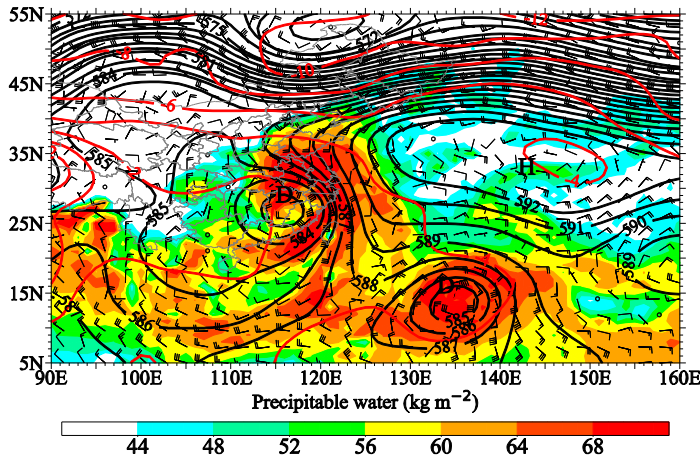
*The typhoon Doksuri_(2305) weakened to a typhoon remnant vortex as it was passing through East China's Anhui Province. The China Meteorological Administration (CMA) stopped issuing updates on the Doksuri at 0300 UTC 29 July 2023. The remnant of Doksuri remained in a vortex in the lower troposphere, although its wind force diminished as it moved northward.

删除的内容: can

删除的内容: at

删除的内容: this

199 shape on its western border. Clearly, a water vapor transportation passage was built due to the
 200 cyclonic circulation of the tropical storm in combination with the anticyclonic circulation on
 201 the southwestern part of the WNPSH. As a result, central and North China was covered by high
 202 precipitable water (PW) of over 68 mm. Similar patterns can be viewed at the level of 850 hPa
 203 (not shown).



204
 205 **Fig. 3** Weather chart on 500 hPa at 1200 UTC 28 July 2023: Geopotential height
 206 (black-contoured at 15 gpm intervals), temperature (red-contoured at 2°C intervals), wind barbs
 207 (a full barb is 4 m s⁻¹), and precipitable water (kg m⁻², shadings).

208 **3. Model configuration and verification**

209 **3.1 Model description**

210 In this study, the persistent severe rainfall event is reproduced with the WRF model
 211 version 4.1.3. The WRF model is configured in two-way nested grids of horizontal grid sizes of
 212 9 km, 3 km, and 1 km. Figure 4 displays the geographical coverage of the WRF model domains,
 213 with the grid points of 901(nx)×601(ny), 973×1231, and 1231×1591 for the outer, intermediate,
 214 and inner domains, respectively. The outermost domain (i.e., D01) is centered at 115°E, 35°N,
 215 and a total sum of 58 sigma levels is assigned in the vertical with the model top fixed at 20 hPa.
 216 Since the rainfall is closely associated with the spatial distribution of orography over North
 217 China (Fig. 1), the Shuttle Radar Topography Mission (SRTM) high-resolution (90 m)
 218 topographic data is employed in the present simulation. It should be noticed that the model
 219 vertical level distribution was carefully tested and has achieved good performance (Yin et al.,
 220 2020; Yin et al.,2022a; Yin et al.,2018; Yin et al.,2022b). The WRF model physics schemes are
 221 configured with the YSU scheme for the planetary boundary layer (Hong et al., 2006), and the

删除的内容: at

删除的内容: heavy

删除的内容: reduplicated

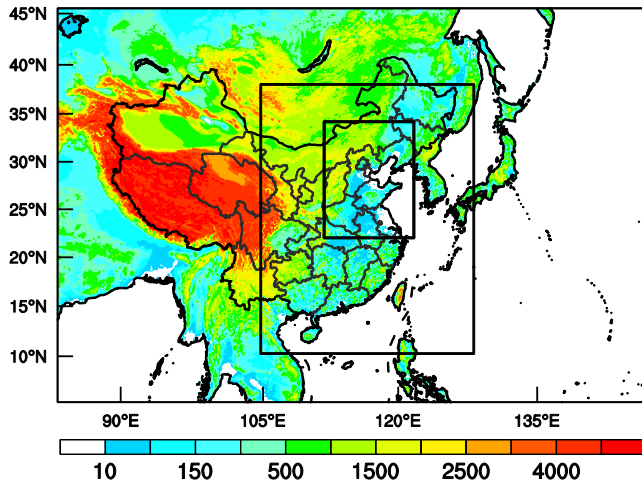
删除的内容: related

删除的内容: to

227 revised MM5 Monin-Obukhov (Jimenez) scheme for the surface layer (Jiménez et al., 2012),
228 as well as the Unified Noah Land Surface Model (Tewari et al.,2004). The rapid radiative
229 transfer model (RRTM) (Mlawer et al.,1997) and the Dudhia scheme (Dudhia,1989) are used
230 for longwave and shortwave radiative flux calculations, respectively. The Kain-Fritsch cumulus
231 parameterization scheme (Kain,2004) is utilized for the outer two coarse-resolution domains
232 but is bypassed in the finest domain (i.e., D03). The Thompson-ensemble cloud microphysics
233 scheme is applied to the explicit cloud processes (Thompson et al.,2008; Yin et al.,2022a).

删除的内容: and

删除的内容: for



234 **Fig. 4** The WRF model orography (m, shadings) and the nested model domains used for
235 simulations with the grid sizes of 9 km (D01), 3 km (D02), and 1 km (D03).
236

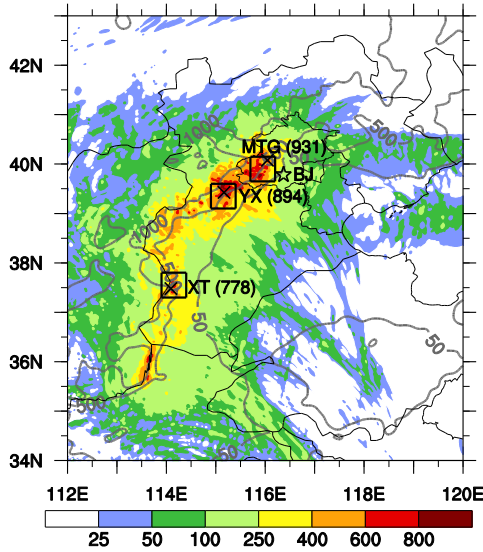
237 The WRF model is integrated for 108 hours, starting from 1200 UTC 28 July 2023, with
238 outputs at 6-min intervals. The model outputs in the first 12 h are considered as the spin-up
239 process and thus are not used for the present work. The initial and outermost boundary
240 conditions are interpolated from the final operational global analysis of 1-degree by 1-degree
241 data at 6-h intervals from the Global Forecasting System of the National Centers for
242 Environment Prediction (NCEP). In order to force large-scale fields consistent with the driving
243 fields, grid analysis nudging is activated by performing the Four-Dimension Data Assimilation
244 (FDDA) throughout the model integration (Bowden et al.,2012; Stauffer et al.,1991). The
245 innermost domain (i.e., D03) outputs are validated and used for further analysis, and the
246 outermost domain (i.e., D01) outputs are used to demonstrate weather-scale dynamical and
247 thermal features. The wind profiler and surface hourly observations are provided by the
248 National Meteorological Information Center (NMIC) of the China Meteorological

删除的内容: Wind

252 Administration (CMA) after strict quality control.

253 3.2 Model verification

254 Figure 5 shows the spatial distribution of 96-h accumulated rainfall from the simulation
255 during the period from 0000 UTC 29 July to 0000 UTC 02 August 2023. Generally speaking,
256 the WRF model replicates well the spatial distribution of severe rainfall. The rainfall belt with
257 three rainfall cores coinciding with the orography is reproduced well, and the simulated
258 extreme rainfall amount matches well with the observed. Note that the model produces a peak
259 96-h accumulated rainfall of 778 mm over the XT region, while the maximum rainfall of 1004
260 mm was observed over the XT region. Despite the simulation underestimates rainfall over this
261 region, it captures the main features of rainfall over central and North China.



262 **Fig. 5** Same as in Fig. 1 but for the simulated rainfall (mm, shadings).

264 Figure 6 compares the spatial distribution of daily rainfalls between observations and
265 simulations during the period from 0000 UTC 30 July to 0000 UTC 2 August 2023. From
266 observations, one can see that the daily rainfalls show obvious variations. On the first day (Fig.
267 6a), the rainfall occurred mainly in northern Henan Province and southern Hebei Province, on
268 the east side of the Taihang Mountains with the rainfall cores over 250 mm. On the next day
269 (Fig. 6b), the rainfall extended significantly northeastward, and a new strong rainfall core
270 occurred, covering central Hebei Province and southwest Beijing. On the third day (Fig. 6c),

删除的内容: heavy

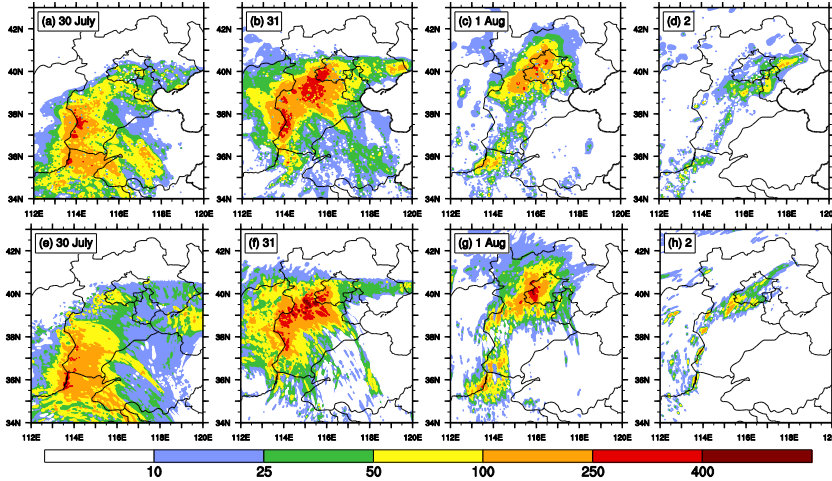
删除的内容: heavy

删除的内容: with three rainfall cores

删除的内容: compares favorably

删除的内容: to

276 rainfall was significantly reduced in both coverage and intensity, mainly occurring in Beijing
 277 and the surrounding areas. On the fourth day (Fig. 6d), rainfall moved eastward and weakened
 278 rapidly. It is apparent that the model reproduces well the evolutions of the rainfall (Fig. 6e-h),
 279 with general characteristics similar to the observed (Fig. 6a-d).



281
 282 **Fig. 6** Spatial distribution of (a-d) observed and (e-h) simulated daily rainfall (mm) during the
 283 period from 0000 UTC 30 July to 0000 UTC 2 August 2023.

284 Figure 7 compares the time series of hourly rainfall rates between the observed and the
 285 simulated over the MTG, YX, and XT regions. The rainfall event is characterized by long
 286 duration, widespread coverage, and high intensity. As has been mentioned above, the rainfall
 287 extended from the south to the north, covering Henan Province, Hebei Province, and Beijing.
 288 The rainfall first occurred in the XT region and ended near 0000 UTC 31 July 2023. In the wake
 289 of that the rainfall belt moved northeastward, over both the MTG and YX regions rainfall
 290 occurred, and it ended nearly at 0000 UTC 2 August. The observed timings of initiating and
 291 ending of the rainfall event are well replicated by the WRF model, with the observed peaks
 292 reproduced as well, although there are some timing biases. For example, the strongest rainfall
 293 occurred over the MTG region during the period from 0000 UTC to 0600 UTC 31 July.
 294 However, the simulated strongest rainfall has a 6-h lag, occurring from nearly 0600 UTC to
 295 1200 UTC 31 July depending on the region. Overall, good agreements between the simulation
 296 and observations are obtained in terms of the timing and location in the spatial distribution of

删除的内容: that are

删除的内容: accumulation

删除的内容: As

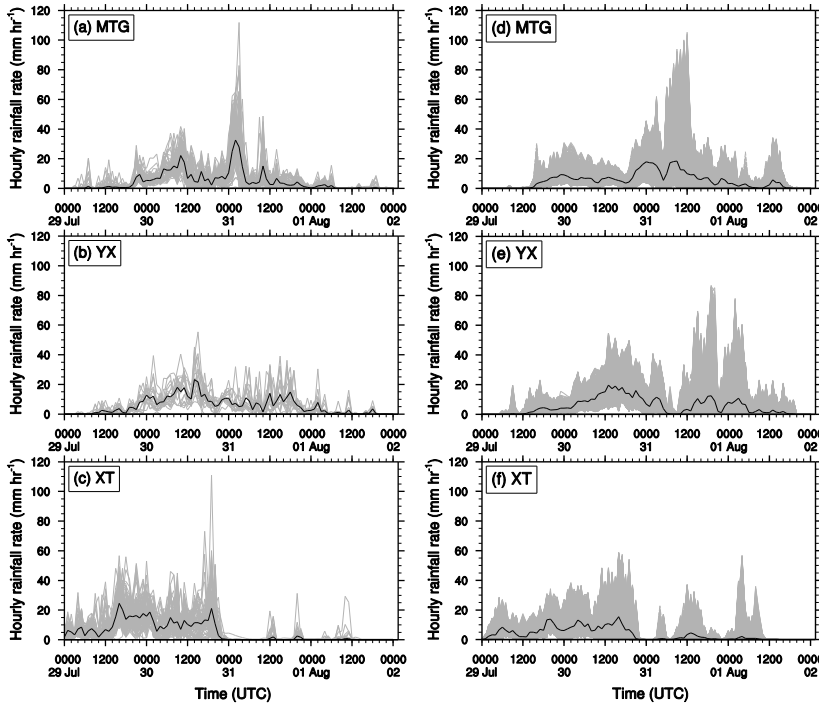
删除的内容: ending

删除的内容: . Besides,

删除的内容: are

删除的内容: errors

304 rainfall.



305
306 **Fig. 7** Time series of (a-c) the rain gauge observations and (d-f) the simulated hourly rainfall
307 rates (gray lines, mm hr⁻¹) for all the stations/grid points over the (a, d) MTG, (b,e) YX, and
308 (c,f) XT regions during the period of 0000 UTC 29 July to 0000 UTC 02 August 2023. The
309 black line denotes the domain-averaged hourly rainfall rates over all the stations (grid points)
310 from observations (simulations). (see Fig. 1 for their locations). In total, 74, 19, and 67
311 observations are used for (a) MTG, (b) YX, and (c) XT, respectively. For the simulation, there
312 are (d) 2296, (e) 2365, and (f) 2420 grid points, respectively.

313 The evolution of the simulated wind profile is presented in Fig. 8. Similar to the observed
314 (Fig. 2), the simulated easterly wind increased gradually from nearly 1200 UTC 29 July,
315 corresponding to the start of the precipitation (Fig. 6e-h). The horizontal wind shifted from
316 easterly to southerly except for near the ground, and then turned to southwesterly with wind
317 speed decreasing significantly. Overall, the variations of the simulated wind profile were
318 consistent with those observed, indicating that the WRF model was able to well capture, the
319 main features of the wind profile. Based on the wind profile and rainfall features, the simulated

删除的内容: simulation

删除的内容: of

删除的内容: .

删除的内容: gradually

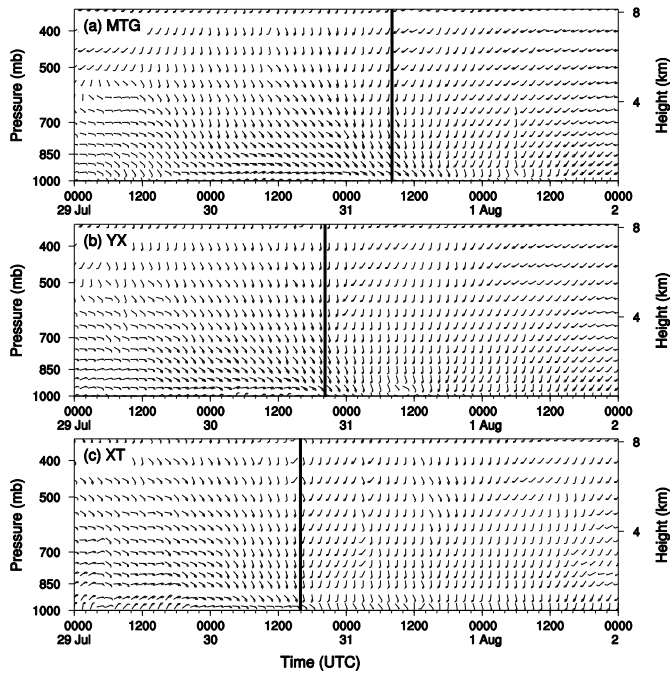
删除的内容: experienced

删除的内容: .

删除的内容: d

327 rainfall process is roughly divided into two stages. The shift moments (roughly marked by thick
 328 black lines) are near at 0800 UTC 31, 2000 UTC 30, and 1600 UTC 30 July for the MTG, YX,
 329 and XT regions, respectively. It should be noted that the wind field was significantly
 330 influenced by Typhoon Khanun (2306) and the remnant vortex originating from Typhoon
 331 Doksuri (2305) in the present event. As the typhoon gradually moved northwestward and the
 332 vortex weakened, the first region to be affected was Xingtai (XT) in the south, then Yixian
 333 (YX) in the center, and finally Mentougou (MTG) in the north, suggesting that the wind shift
 334 occurred at a different moment.

删除的内容: . Therefore,
 删除的内容: s



335
 336 **Fig. 8** Same as Fig. 2 but for the simulated. The black lines denote wind shift from
 337 southeasterly to southerly/southwesterly over the levels in the low to middle troposphere,
 338 which roughly divided the rainfall event into two stages.

339 **4. Unique features for the extreme rainfall**

340 **4.1 Dominant dynamic processes for convection initialization**

341 The evolution of dynamical and thermal systems of the rainfall event in the first stage is
 342 shown in Fig. 9. Although only a remnant vortex remained over central China at this time,
 343 typhoon Doksuri had an important influence on the W_NPSH when it was strong as a super

346 typhoon. Several days before the rainfall event, the super typhoon Doksuri was close to the
347 W~~N~~PSH, and the southwest W~~N~~PSH edge was within the typhoon's outer region. Owing to the
348 inflow mass flux entering the typhoon region, ~~the southwest part of W~~N~~PSH was severely~~
349 ~~weakened~~ by typhoon Doksuri (Sun et al.,2015). As a result, the west boundary of the W~~N~~PSH
350 appeared to an eastward retreat from 500 hPa to 850 hPa, showing an inclined vertical
351 distribution on ~~its~~ western boundary, especially from 700 hPa to 850 hPa. Capped by the
352 inclined W~~N~~PSH, water vapor was mainly transported to North China through a passage nearly
353 under 850 hPa ~~that~~ is built by the typhoon remnant vortex ~~combined with~~ the tropical storm
354 Khanun. At 500 hPa (Fig. 9a), the W~~N~~PSH (represented by the 588 isoline) covered a large part
355 of eastern China, with an unusual westward extension of the northwest corner to northwest~~ern~~
356 China. ~~At that time, the~~ northwest corner extended much further westward, compared to that
357 before 12-h (Fig. 3). Similar patterns can be seen at 700 hPa (Fig. 9b), but the west boundary of
358 W~~N~~PSH (represented by the 316 isoline) retreated to the East China Sea except for the
359 northwest corner. At 850 hPa (Fig. 9c), the W~~N~~PSH (represented by the 156 isoline) completely
360 retreated to the ~~Western North~~ Pacific, far away from China.

361 The spatial distribution of the high PW was consistent with that of a large equivalent
362 potential temperature (θ_e) of 344K at 500 hPa, indicating that the 334K contour covered a
363 relatively warm and/or wet region (Fig. 9a). Most important~~ly~~, the boundary of the high PW
364 corresponded to the large value of the potential temperature gradient over 8K on the east side
365 and 12K on both north and west sides. Previous studies (e.g., Rao et al.,2023) proposed that the
366 heavy rainfall region was closely attributed to the distributions of θ_e . Although the warm and
367 moist conditions were favorable for precipitation, the unfavorable large-scale forcings explain
368 well why no deep convection was formed over this region (marked with a dashed-line box in
369 Fig. 9c, ~~d~~). The convergence, resulting from changes in wind direction and wind speed, was
370 conducive to triggering convection. Consequently, the weak convergence led to weak lifting
371 and consequent precipitation. Since the convergence occurred at the junction of cold and warm
372 air masses, like a warm front rainfall, rainfalls were formed in low intensity but long duration
373 and widespread coverage. It is important to note that the spatial distribution of rainfall is usually
374 considered to be consistent with the western boundary of W~~N~~PSH (i.e., the 588 isoline) at 500
375 hPa. However, the spatial distribution of rainfall in the present event is consistent with the dense
376 zone of θ_e , instead of the ~~western boundary of~~ W~~N~~PSH. Therefore, in addition to the isoline 588

删除的内容: and thus

删除的内容: destroyed

删除的内容: the

删除的内容: which

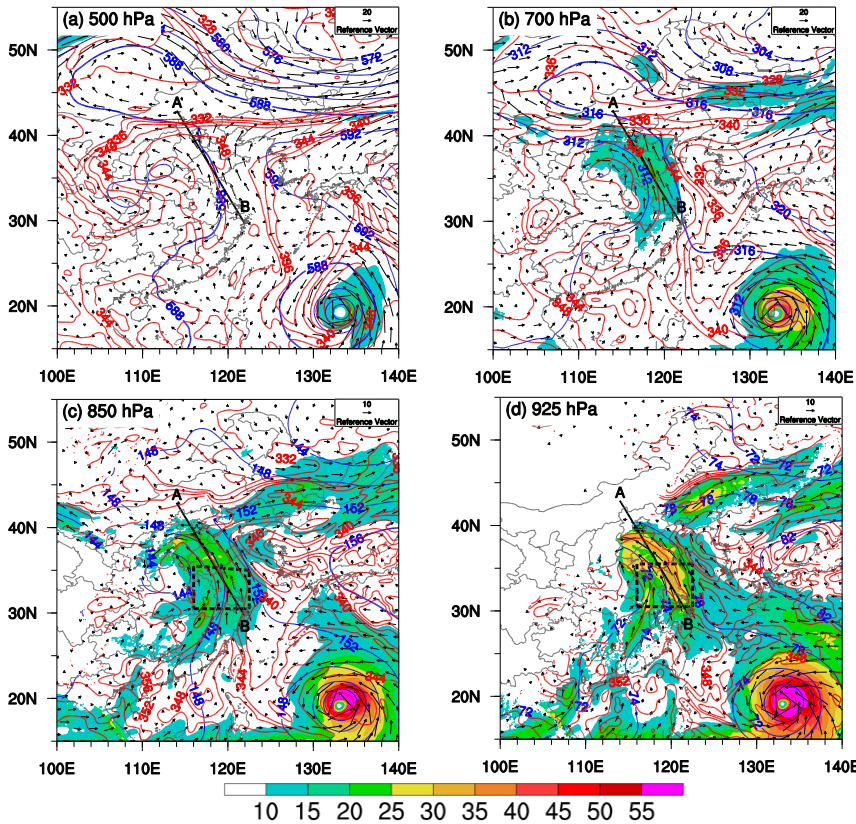
删除的内容: and

删除的内容: The

删除的内容: w

删除的内容: which was

385 at 500 hPa, the spatial distribution of θ_e needs to be given more attention in future operational
 386 forecasts.



387 **Fig. 9** Spatial distribution of geopotential height (blue contoured at 40 gpm), equivalent
 388 potential temperature (red contoured at 2K intervals, θ_e), wind bars (a full barb is 4 m s⁻¹), and
 389 water vapor flux (g s⁻¹ cm⁻¹ hPa⁻¹, shadings) from the model D01 at 0000 UCT 30 July 2023: (a)
 390 500 hPa, (b) 700 hPa, (c) 850 hPa, and (d) 925 hPa. The isolines of 588, 316, and 156 are
 391 bolded to represent the W_NPSH at 500 hPa, 700 hPa, and 850 hPa, respectively. The
 392 convergence zone of southeast and southwest flows is marked by a dashed line box in panels (c)
 393 and (d). The thick black line A–B denotes the locations for cross-section along the water vapor
 394 transport pathway used in Fig. 10.

395 The warm and moist features over North China can also be seen from the cross-section
 396 along the line A–B as shown in Fig. 10. The western orography region was occupied by cold air
 397 mass over the levels above 3.0 km. Under the conditions, significant equivalent potential
 398 temperature gradients were established between the warm and cold air masses, similar to a

删除的内容: and

删除的内容: controlled

401 warm front. Meanwhile, owing to the blocking of orography below 1.3 km and the strong cold
402 air mass above 3.0 km, only the southeasterly flows between 1.3 and 3.0 km above the sea level
403 can overpass the mountains. It should be noted that although the warm and moist southeasterly
404 flows were lifted by the orography, they could not move further upward to trigger convection
405 because of the local capped cold and dry air masses overhead. Consequently, convergence
406 mainly resulted from the changes in wind direction and wind speed caused upward motion. As
407 the warm and moist air was lifted, condensation occurred and even generated precipitation. It
408 should be emphasized that the lifting was too weak to allow convection to be highly organized
409 (Fig. 10). For example, the updrafts in strong deep convective systems (e.g., Yin et al.,2020;
410 Yin et al.,2022c) are 5-10 times as large as the updrafts in the present event. Therefore, the weak
411 lifting was responsible for the rainfall in large coverage but low intensity. Besides, the
412 continuous and stable water vapor supply was another favorable factor for the precipitation.

413 Also from Fig. 10, one can see that North China was surrounded by warm dry air masses
414 on the east side and cold dry air masses on both north and west sides. More specifically, the air
415 mass at the levels above 1 km on the east side was over 3°C warmer than surrounding regions,
416 but the water vapor mixing ratio (q_v) was less than 14 g kg⁻¹ (humidity was less than 70%)
417 because this region was controlled by the WNPSH. The warm-dry cap overhead explains well
418 the absence of convection and rainfall over this region (cf. Figs. 5 and 6). On the north and west
419 sides, the air masses were dry with q_v less than 2 g kg⁻¹. The air was over 3°C colder than the
420 surrounding region except for the air near the ground. In view that warm air near the ground
421 might be associated with radiative heating from the ground, owing to being capped by the cold
422 and dry air overhead, it would be understandable why convection could not be enhanced over
423 the mountains.

删除的内容: led to

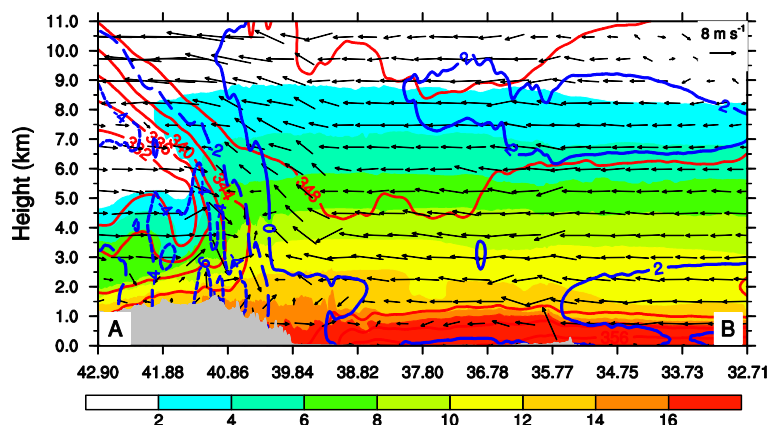
删除的内容: thus

删除的内容: Note

删除的内容: . C

删除的内容: explains

删除的内容: advanced



430
 431 **Fig. 10** Vertical cross-section along line A–B given in Fig. 9 of temperature deviations
 432 (blue-contoured at 2°C intervals) from their level-averaged values in the cross-section,
 433 equivalent potential temperature (red-contoured at 4K intervals), water vapor mixing ratio (q_v ,
 434 g kg^{-1} , shadings), and in-plane flow vectors (vertical motion amplified by a factor of 20) at 0000
 435 UCT 30 July 2023, respectively. Gray shadings denote terrain.

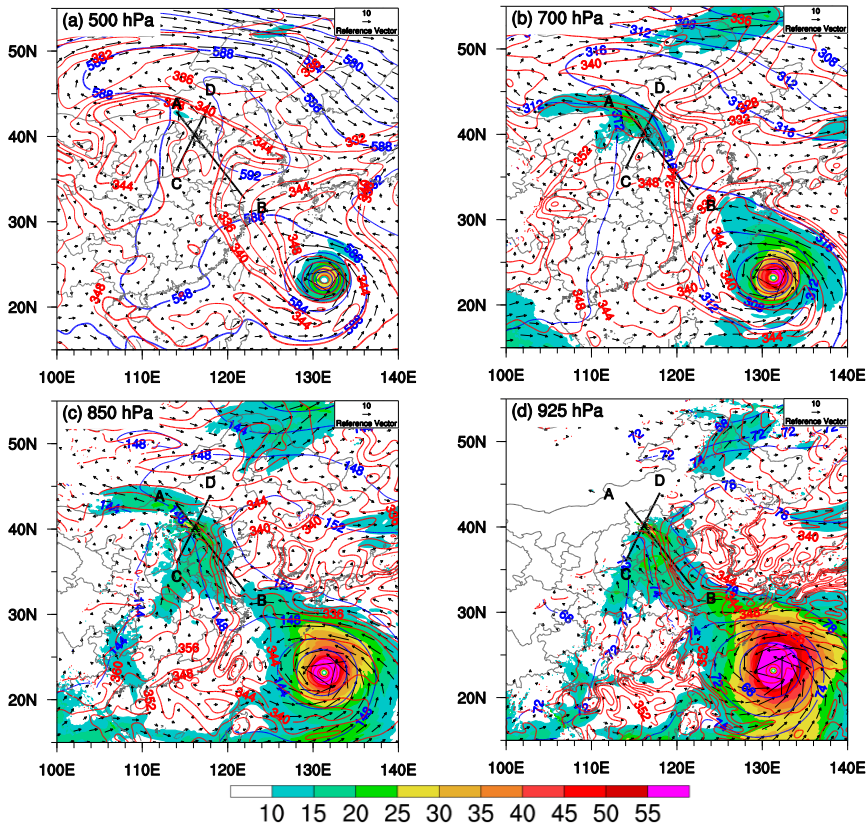
436 In the second stage (Fig. 11), obvious differences in dynamical and thermal processes can
 437 be seen, compared to those in the first stage (cf. Fig. 9). At 500 hPa (Fig. 11a), the W_NPSH
 438 further expanded westward with its western border reaching western China. It should be
 439 emphasized that the southwest_{ern} part of W_NPSH was severely damaged by the rapid
 440 intensification of Khanun into a super typhoon. Meanwhile, as the trough deepened over
 441 northeastern China, cold air from the north poured southward. Consequently, a north-south
 442 orientated θ_e dense zone was established over east_{ern} China. Similar patterns in θ_e and
 443 horizontal wind field can be seen at 700 hPa (Fig. 11b). However, the W_NPSH (represented by
 444 the 316 isoline) was further disrupted as the Khanun continued to intensify, appearing that the
 445 W_NPSH retreated to the East China Sea except for the northwest corner. The north-south
 446 orientated θ_e dense zone greatly prevented water vapor from transporting to North China above
 447 850 hPa, and thus water vapor was mainly transported to North China by a shallow
 448 southeasterly flow near the ground (Fig. 11c, d). Consequently, the water vapor flux was
 449 significantly reduced (Fig. 12a). Besides, North China was dominated by southerly flows over
 450 levels above 500 hPa, and thus mid-tropospheric wind shear was significantly enhanced.

删除的内容:

删除的内容: viewed

删除的内容: ern

删除的内容: ern



455 **Fig. 11** Same as Fig. 9 but for 0800 UTC 31 July 2023. Thick black lines A–B and C–D denote
 456 the locations for the cross-section in Fig. 12.

457 As addressed above, it was the variation in environmental conditions that caused
 458 consequent rainfall changes in nature. Especially, the shift in the wind field brought changes
 459 in thermodynamic processes and water vapor sources. Before the wind shift (Figs. 9 and 10),
 460 water vapor was mainly from the East China Sea associated with the cyclonic circulation of
 461 the typhoon remnant vortex and the tropical storm Khanun and southeasterly flow below 925
 462 hPa. After the shift, water vapor flux was significantly reduced from both southwesterly and
 463 southeasterly flows (Fig. 11). Under such a framework, convections were largely triggered by
 464 orographic blocking and lifting of southerly/southwesterly flows as convective instability air
 465 approached the orography (Fig. 12). Unlike in the first stage, convections were further
 466 developed northward over mountains, forming deep convections (Fig. 12b), which might be

删除的内容: s

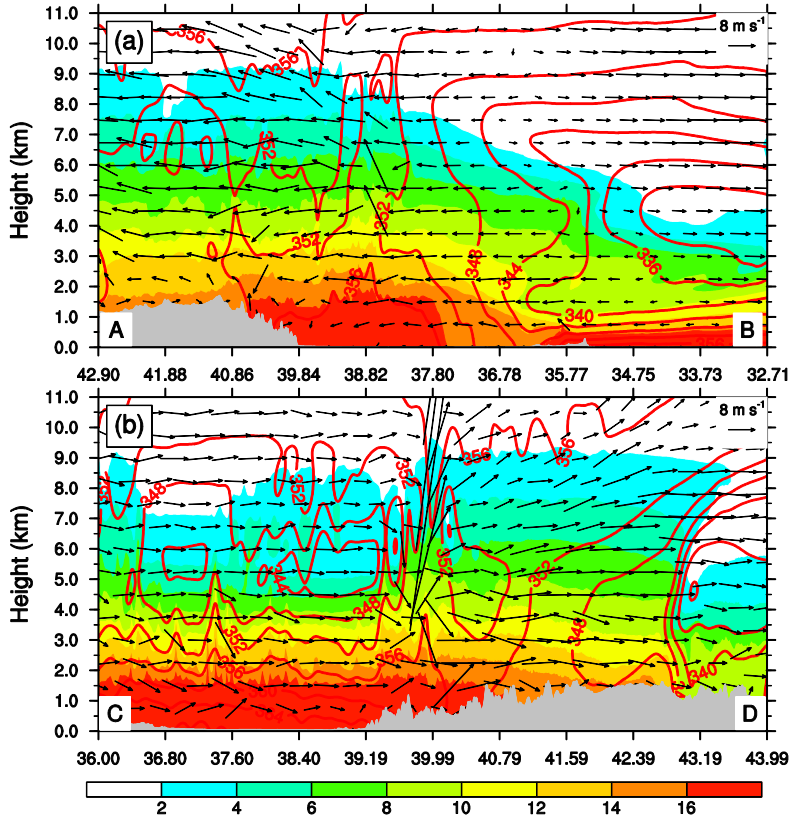
删除的内容: the

删除的内容: northward

删除的内容: . One of the reasons is

471 attributed to the fact that the cold air on the north side moved northward. Generally speaking,
 472 the convections in the second stage are much stronger and deeper than those in the first stage.
 473 Consequently, the rainfall intensity is increased, compared to those in the first stage (Figs.
 474 7d,e).

删除的内容: Comparatively



475
 476 **Fig. 12** Vertical cross-sections along lines (a) A–B and (b) C–D given in Fig. 11 of equivalent
 477 potential temperature (θ_e , red-contoured at 4K intervals), water vapor mixing ratio (q_v , g kg⁻¹,
 478 shadings), and in-plane flow vectors (vertical motion amplified by a factor of 10) at 0800 UCT
 479 31 July 2023. Gray shadings denote terrain.

删除的内容:

481 **4.2 Moisture budget**

482 The shift in wind direction and speed implies a change in water vapor source and rainfall
 483 properties (Fig. 13). As stated above, water vapor was mainly from the East China Sea
 484 associated with the cyclonic circulation of typhoon Khanun before the wind shift, and was

487 fueled by the southeasterly flow below 925 hPa. After the shift, the water vapor supply was
488 significantly reduced due to both southwesterly and southeasterly flow variations. Figure 13
489 shows the time-height cross-sections of moisture flux across eastern, southern, western, and
490 northern boundaries and total lateral boundary moisture flux for the MTG region. The
491 moisture flux is calculated by

$$QFlux = \int_0^L q_v \bar{v} dl .$$

492
493 Here, $QFlux$ is moisture flux across one of the four boundaries, and q_v , \bar{v} , and L are water
494 vapor mixing ratio, wind vector, and the length of the boundary, respectively. The TOT is a
495 summation of the $QFlux$ s from the four boundaries by taking inward (outward) as positive
496 (negative).

497 One can see that the MTG region experienced vigorous lower-to-middle level inward
498 (outward) moisture fluxes across their eastern and southern (western and northern) boundaries.
499 For the eastern boundary (Fig. 13a), the inward moisture flux began to increase gradually from
500 0000 UTC 29 July, with the maximum values over $13,500 \text{ kg kg}^{-1} \text{ m}^2 \text{ s}^{-1}$ occurring between
501 1200 UTC 30 and 0000 UTC 31 July 2023. Then, the inward flux moisture decreased rapidly
502 and even transformed to the outward flux at 0000 UTC 1 August 2023. The inward moisture
503 flux was mainly concentrated below 3 km above the sea level because upper levels were capped
504 by the warm dry air masses associated with the W_NPSH (cf. Figs. 9 and 10) movement.
505 However, owing to weak lifting over, most of the water vapor flowed out through the western
506 boundary (Fig. 13b). Meanwhile, part water vapor was transported in this region from the
507 southern boundary except for the lower levels during 0000 UTC 30 to 0000 UTC 31 July 2023
508 (Fig. 13d). The outward flow water vapor is caused by the northeasterly branch around flow
509 due to the blocking of the Yanshan Mountains. Similar patterns can be found in the northern
510 boundary with almost the same outward water vapor flux (Fig. 13c). The temporal evolution of
511 the water vapor flux across the eastern boundary is consistent with that of rainfall over this
512 region (Figs. 13a and 7d), suggesting that rainfall formation was dominated by the inward of
513 water vapor from the eastern boundary. Overall, the inward net moisture fluxes were
514 concentrated in the lower troposphere between 0.5 km and 1.5 km (Fig. 13e), suggesting that

删除的内容: from

删除的内容: s

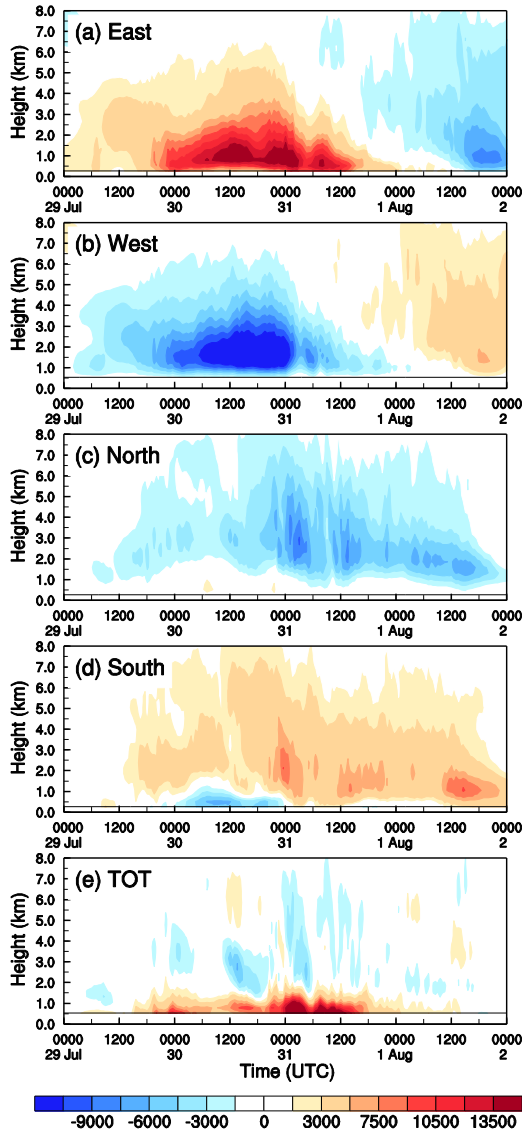
删除的内容: as

删除的内容: resulted from

删除的内容: seen

520 most of the water vapor was consumed at this layer by condensation. Despite the high water
 521 vapor flux, the water vapor-rich layer is too thin (nearly 1 km) to be favorable for the formation
 522 of severe rainfall. Similar patterns can be found over both YX and XT regions (not shown),
 523 although there were temporal and quantitative differences.

删除的内容: heavy



524 Fig. 13 Time-height cross-sections of the moisture fluxes ($\text{kg kg}^{-1} \text{m}^2 \text{s}^{-1}$) through the (a)
 525 eastern, (b) western, (c) northern, and (d) southern boundaries of the MTG region in Fig. 1; (e)
 526

删除的内容: cross

529 TOT provides the total net moisture flux of all boundaries.

530 In the second stage, the north-south orientated θ_e dense zone greatly prevented water vapor
531 from being transported to North China by southeasterly flows from the East China Sea, and thus
532 water vapor was mainly transported to North China across the south boundary (Figs. 13b,d).
533 Unlikely, the water vapor was mainly provided by southeasterly_(southwesterly) flow
534 below(above) 500 hPa. Figure 13 shows the time-height cross-sections of the moisture fluxes.
535 It is seen from Fig. 13 that the water vapor flux amount was significantly reduced. Despite the
536 thickening of the water vapor flux layer associated with the southerly/southwesterly flows, the
537 water vapor flux is much less, compared to the first stage. Therefore, the wind shift had strong
538 effects on the reduction in water vapor flux and consequent rainfall over North China. The same
539 results can also be obtained in the YX and XT regions (not shown). It is worth emphasizing that
540 strong hourly rainfalls occurred during the wind shift period (cf. Figs. 2, 7, and 8), suggesting
541 that the changes in wind direction enhanced wind shear and thus promoted the development of
542 convections and consequent precipitation under moisture and instability conditions (Chen et al.,
543 2015; Rotunno et al.,1988; Schumacher and Rasmussen,2020). Therefore, it is important to pay
544 special attention to environmental wind alterations in future remote rainfall forecasts.

545 **4.3 Properties of convection**

546 Figure 14 shows the temporal evolution of maximum upward motion and radar reflectivity
547 over the MTG region during the rainfall period from 0000 UTC 29 to 0000 UTC 2 August 2023.
548 In the first stage (i.e., before 0800 31 July), most of the maximum updrafts were almost less
549 than 3 m s^{-1} . Owing to the weak updrafts, the storm did not stretch as high as typical convective
550 systems over North China, with hydrometeors concentrated on the levels with a temperature
551 above 0°C (Fig. 14a). As addressed above (Fig. 10), weak updrafts were attributed by the
552 unfavorable large-scale conditions. The vertical distribution of hydrometeor indicates that the
553 warm rain processes were dominant in the persistent rainfall event. The result is consistent with
554 the water vapor consumed layer between 0.5 km and 1.5 km (Fig. 13e). Unlikely, the maximum
555 updraft was over 11 m s^{-1} in the second stage (i.e., after 0800 31 July), which is much stronger
556 than that in the first stage (Fig. 14). Correspondingly, the radar reflectivity penetrated through
557 the 0°C level with a cloud top exceeding 12 km, indicating that both warm and cold rain

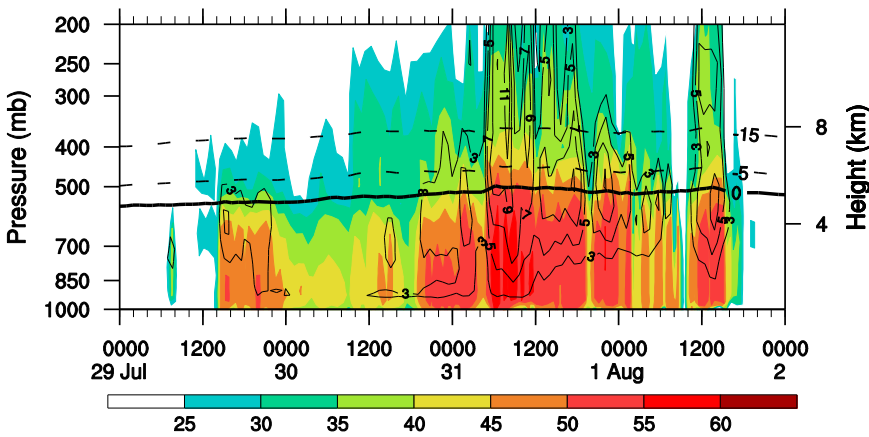
删除的内容: Note

删除的内容: (Fig. 13)

560 processes were active in this stage. Correspondingly, the intensity of hourly rainfall increased
 561 significantly, with the maximum value exceeding 100 mm (Fig. 7d). Generally speaking, there
 562 are larger strong convective areas in the second than those in the first stage. The same features
 563 were also found in the regions of YX and XT (not shown). Unlike the usual short-duration
 564 heavy rainfall in North China (Mao et al.,2018; Xia and Zhang,2019; Yin et al.,2022b; Li et
 565 al., 2024), this precipitation was mainly dominated by warm cloud processes (Fig. 14),
 566 consistent with observations (e.g., Fu et al., 2023). As addressed above, the weak updrafts
 567 with warm-moist air were responsible for persistent rainfall but low intensity. A detailed
 568 analysis of cloud microphysical processes for this event will be given in a forthcoming study,
 569 in which all microphysical source and sink terms will be explained.

删除的内容: Comparatively

删除的内容: but



570
 571 **Fig. 14** Time-height cross-section of domain maximum radar reflectivity (dBz, shadings) and
 572 upward motion (contoured at 2 m s^{-1}) taken from MTG region during the period from 0000
 573 UTC 29 to 0000 UTC 2 August 2023. The isothermal lines denote the 0°C (the melting layer),
 574 -5°C , and -15°C levels, respectively.

删除的内容: dBZ

带格式的: 突出显示

575 **5. Conclusions and outlook**

576 In this study, we examined the convective initiation and subsequent persistent heavy
 577 rainfall over North China during the period from 29 July to 2 August 2023 in terms of
 578 observations and simulations with the WRF model. From observations, the rainfall was
 579 featured by long duration and widespread coverage but low intensity, like a warm front rainfall.
 580 Firstly, the persistent severe rainfall event was reproduced by the WRF model. Further

删除的内容: with

删除的内容: heavy

带格式的: 突出显示

586 analysis based on the simulations shows that this persistent precipitation was caused by a
587 combination of a remnant vortex originating from typhoon Doksuri_(2305), the tropical storm
588 Khanun_(2306), the Western North Pacific subtropical high (WNPSH) with an unusual
589 westward extension of the northwestern corner, and stable cold dry air from over northern
590 China.

删除的内容: w

591 According to the simulated wind profiles and rainfall features, the persistent heavy rainfall
592 event was divided into two stages. Figure 15 summarizes the synoptic-scale forcings and
593 possible dynamic mechanisms for the persistent heavy rainfall. In the first stage (Fig. 15a), a
594 water vapor transportation passage was built by a typhoon remnant vortex and a tropical storm
595 Khanun, providing a stable warm moist water vapor supply. Several days before the rainfall
596 event, the southwestern WNPSH was within the typhoon Doksuri's outer region, and thus the
597 southwestern WNPSH was weakened by the tropical storm Doksuri. It appears that the west
598 boundary of the western North Pacific subtropical high (WNPSH) retreated eastward from 500
599 hPa to 850 hPa, showing an inclined vertical distribution on the western boundary, especially
600 from 700 hPa to 850 hPa. Capped by the inclined WNPSH, water vapor was mainly transported
601 to North China through a water vapor passage under nearly 850 hPa (Fig. 10). Although the
602 warm and moist regions were favorable for precipitation over North China, organized strong
603 convective systems were seldom because of the absence of favorable large-scale conditions. At
604 the same time, the orography in the western part of North China was occupied by dry cold air
605 mass over levels above 3.0 km. Owing to the blockings of orography below 1.3 km and the
606 strong cold air mass above 3.0 km, only the southeasterly flows between 1.3 and 3.0 km above
607 the sea level can overpass the mountains. Although the warm and moist southeasterly flows
608 were lifted by the orography, they could not go further upward to trigger convections because of
609 the locally capped cold and dry air masses overhead. Under the conditions, significant
610 equivalent potential temperature gradients were established between the warm and cold air
611 masses, similar to a warm front. Consequently, convergence mainly resulted from the changes
612 in wind direction and wind speed led to upward motion. As the warm and moist air was lifted,
613 condensation occurred and further generated precipitation. However, the lifting was too weak
614 to allow convection to be highly organized (Fig. 14), leading to the rainfall in low intensity but

删除的内容: destroyed

删除的内容: un

删除的内容: controlled

删除的内容: thus

620 large coverage. Besides, the continuous and stable transportation of water vapor provided by
621 tropical storm Khanun ensured stable precipitation over a long period of over 80 h. Therefore,
622 this event shows similar rainfall features to those of a warm front rainfall with a long duration
623 and widespread coverage but low intensity.

624 In the second stage (Fig. 15b), the W~~N~~PSH further expanded westward at 500 hPa, with its
625 western border reaching western China. However, the southwest part of W~~N~~PSH was further
626 damaged by the rapid intensification of Khanun into a super typhoon. Consequently, the
627 embedded warm-dry cover associated with the tilted W~~N~~PSH was significantly thinned,
628 favoring convective development. Meanwhile, as the trough deepened over northeastern China,
629 cold air from the north poured southward. Consequently, a north-south-orientated equivalent
630 potential temperature (θ_e) dense zone was established over eastern China, which greatly
631 prevented water vapor from being transported to North China (Fig. 12a). However, owing to the
632 clockwise rotated southeasterly flow, a deep southerly/southwesterly flow was built over North
633 China. ~~The convections~~ were triggered by orographic blocking and lifting of
634 southerly/southwesterly flows as convective instability air approached orography. Unlike the
635 first stage, the convections were further developed ~~northward~~ over mountains, forming deep
636 convections. It should be noted that the northward-moved cold air on the north side was
637 another favorable condition. Therefore, the convections in the second stage are much stronger
638 and deeper than those in the first stage, although water vapor flux is smaller ~~in the second~~
639 period. Consequently, the rainfall intensity is increased, compared to that in the first stage.
640 Correspondingly, both warm and cold rain processes were active in the second stage, while
641 warm rain processes were dominant in the first stage.

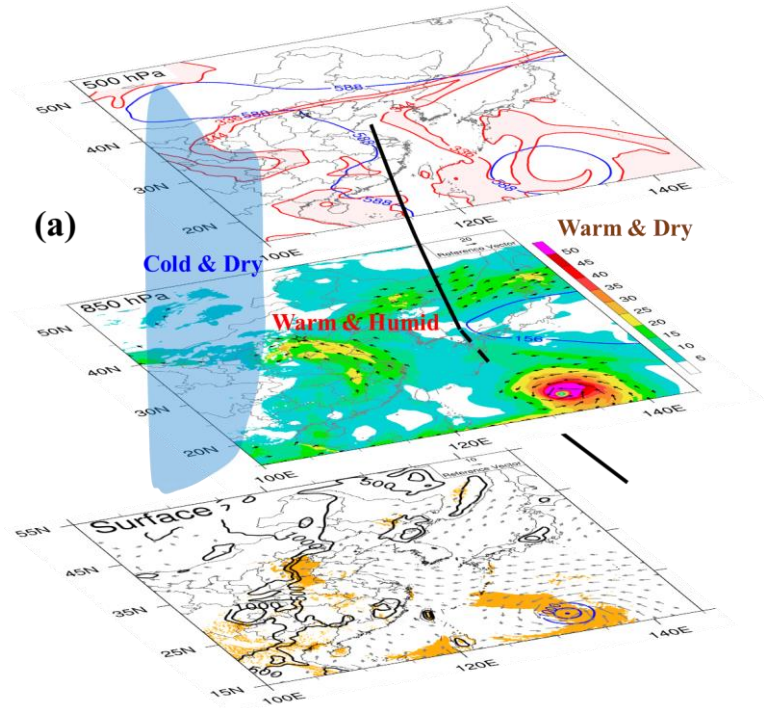
删除的内容: (

删除的内容:)

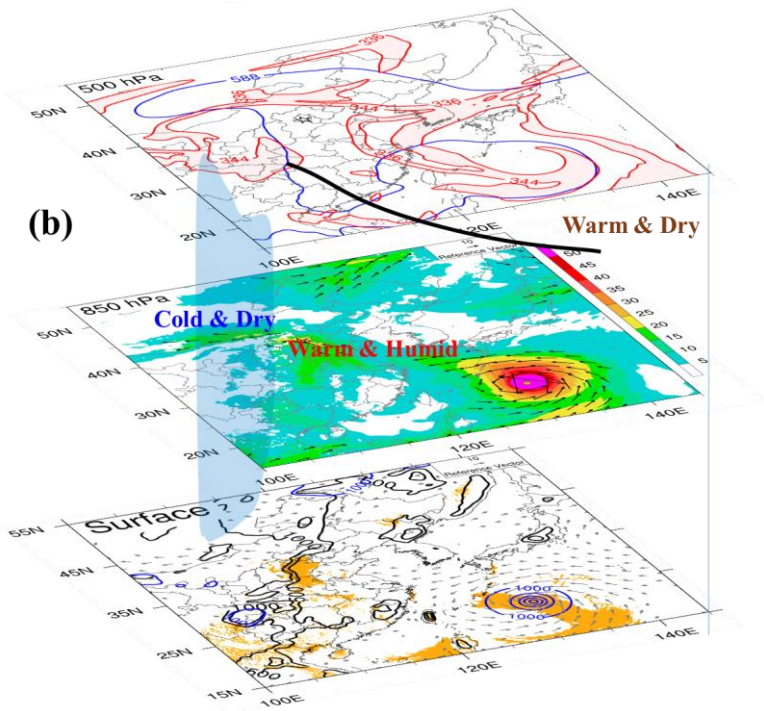
删除的内容: Convections

删除的内容: northward

删除的内容: than



647



648

649 **Fig. 15** (a) Three-dimensional diagram of the mechanisms for the persistent heavy
650 precipitation in the first stage. Several distinct synoptic systems, including the tropical storm
651 Khanun_(2306), a remnant vortex originating from the typhoon Doksuri_(2305),
652 quasi-stationary cold dry air masses, and an abnormal Western North Pacific subtropical high
653 (WNPSH) with inclined vertical distribution on the western boundary (thick black line). Blue
654 lines marked with 588 and 156 represent the WNPSH at 500 hPa and 850 hPa, respectively.
655 Red lines denote the spatial distribution of equivalent potential temperature (θ_e) dense zone
656 between 336 K and 344K. At 850 hPa, black arrows indicate jets with wind speed over 12 m
657 s^{-1} , and shadings denote water vapor flux. Orange shadings imply 96-h accumulated rainfall
658 over 200 mm; blue contours denote sea level pressure; gray arrows denote surface (i.e., $z=10$
659 m) horizontal wind with wind speed over 5 $m s^{-1}$, and black contours indicate orography (m).
660 (b) Same as (a) but for rainfall in the second stage.

删除的内容: w

661
662 In this study, we have gained principal results of the persistent heavy rainfall event. It is
663 important to note that the spatial distribution of rainfall is usually considered to be consistent
664 with the western boundary of WNPSH (i.e., the 588 isoline) at 500 hPa. In the present event, the
665 spatial distribution of rainfall is consistent with the dense zone of θ_e , rather than the western
666 boundary of WNPSH. Therefore, in addition to the 588 isoline, the spatial distribution of θ_e
667 needs to be given more attention in future operational forecasts. Besides, we should give weight
668 to environmental wind shifts, which may lead to changes in convections and the nature of
669 consequent precipitation. Although reasonable dynamic mechanisms for the present persistent
670 heavy rainfall have been proposed, there are still several questions that need to be answered.
671 Among those, more work is required to understand detailed cloud and precipitation processes.
672 In addition, diagnostic and budget analyses will be conducted to understand how the orography
673 facilitates the generation of the rainfall belt with three rainfall cores along the mountains.
674 Nevertheless, the concept of synoptic-forcing-based forecasting is discussed as it might apply
675 to a broader spectrum of forecast events than just over North China.

676
677 **Code and data availability**
678 The source code of the Weather Research and Forecasting model (WRF v4.1.3) is available at
679 <https://github.com/wrf-model/WRF/releases> (last access 1 August 2024). The National

681 Centers for Environmental Prediction (NCEP) Global Forecast System one-degree final
682 analysis data at 6 h intervals used for the initial and boundary conditions for the specific
683 analyzed period can be downloaded at <https://rda.ucar.edu/datasets/d083002/> (last access 1
684 August 2024). Modified WRF model codes and all the data used in this study are available
685 from the authors upon request.

686

687 **Author contributions**

688 Conceptualization: JY, JS, and XL; methodology: JY and JS; data curation: JY and FL;
689 writing – original draft preparation: JY, and FL; writing – review and editing: JY, ML, RX,
690 XB, and JS; project administration: XL; funding acquisition: JY and XL. All authors have
691 read and agreed to the published version of the paper.

692

693 **Competing interests**

694 The contact author has declared that none of the authors has any competing interests.

695

696 **Acknowledgments**

697 The authors acknowledge the use of the NCAR Command Language (NCL) in the preparation
698 of figures.

699

700 **Financial support**

701 This study is jointly supported by the National Key R&D Program of China
702 (2022YFC3003903), National Natural Science Foundation of China (42075083), Open Project
703 Fund of China Meteorological Administration Basin Heavy Rainfall Key Laboratory
704 (2023BHR-Z03), Basic Research Fund of Chinese Academy of Meteorological Sciences
705 (2023Z001), and the Development Foundation of Chinese Academy of Meteorological
706 Sciences (2019KJ026).

References

- 707
- 708 Bao, X., Sun, J., Yin, J., Gao, X., Li, F., Liang, X., Gu, H., Xia, R., Li, M., Wu, C., and Feng,
709 J.: What Caused the Differences between “23·7” and “96·8” Extreme Rainfall Events in
710 North China under a Similar Synoptic Background?, *Journal of Meteorological Research*,
711 38, 861-879, <https://doi.org/10.1007/s13351-024-3192-0>, 2024.
- 712 Bowden, J. H., Otte, T. L., Nolte, C. G., and Otte, M. J.: Examining Interior Grid Nudging
713 Techniques Using Two-Way Nesting in the WRF Model for Regional Climate Modeling, *J.*
714 *Clim.*, 25, 2805-2823, <https://doi.org/10.1175/JCLI-D-11-00167.1>, 2012.
- 715 Chen, Q., Fan, J., Hagos, S., Gustafson Jr, W. I., and Berg, L. K.: Roles of wind shear at
716 different vertical levels: Cloud system organization and properties, *Journal of Geophysical*
717 *Research: Atmospheres*, 120, 6551-6574, <https://doi.org/10.1002/2015JD023253>, 2015.
- 718 Ding, Y.: A case study on the excessively severe rainstorm in Honan province, early in August,
719 1975, *Scientia Atmospherica Sinica*, 2, 276-289. (in Chinese), 1978.
- 720 Dudhia, J.: Numerical Study of Convection Observed during the Winter Monsoon Experiment
721 Using a Mesoscale Two-Dimensional Model, *Journal of the Atmospheric Sciences*, 46,
722 3077-3107, [https://doi.org/10.1175/1520-0469\(1989\)046<3077:NSOCOD>2.0.CO;2](https://doi.org/10.1175/1520-0469(1989)046<3077:NSOCOD>2.0.CO;2),
723 1989.
- 724 Feng, W. and Cheng, L.: Nonhydrostatic numerical simulation for the "96.8" extraordinary
725 rainstorm and the developing structure of mesoscale system, 16, 423-440, 2002.
- 726 Fowler, H. J., Blenkinsop, S., Green, A., and Davies, P. A.: Precipitation extremes in 2023,
727 *Nature Reviews Earth & Environment*, 5, 250-252,
728 <https://doi.org/10.1038/s43017-024-00547-9>, 2024.
- 729 Fu, J., Quan, W., Mai, Z., Luo, Q., Chen, T., Li, X., Xu, X., Zhu, W., Hua, S., and Han, X.:
730 Preliminary study on the refined characteristics of rainfall intensity and dynamic and
731 thermodynamic conditions in the July 2023 severe torrential rain in north China,
732 *Meteorological Monthly*, 49, 1435-1450, 10.7519/j.issn.1000-0526.2023.112701, 2023.
733 (In Chinese with English abstract)
- 734 Gao, Z., Zhang, J., Yu, M., Liu, Z., Yin, R., Zhou, S., Zong, L., Ning, G., Xu, X., Guo, Y., Wei,

735 H., and Yang, Y.: Role of Water Vapor Modulation From Multiple Pathways in the
736 Occurrence of a Record-Breaking Heavy Rainfall Event in China in 2021, *Earth and Space*
737 *Science*, 9, e2022EA002357, <https://doi.org/10.1029/2022EA002357>, 2022.

738 Gao, X., Sun, J., Yin, J., Abulikemu, A., Wu, C., Liang, X., and Xia, R.: The impact of
739 mountain-plain thermal contrast on precipitation distributions during the “23·7”
740 record-breaking heavy rainfall over North China, *Atmospheric Research*, 107582,
741 <https://doi.org/10.1016/j.atmosres.2024.107582>, 2024.

742 Hirata, H. and Kawamura, R.: Scale interaction between typhoons and the North Pacific
743 subtropical high and associated remote effects during the Baiu/Meiyu season, *Journal of*
744 *Geophysical Research: Atmospheres*, 119, 5157-5170,
745 <https://doi.org/10.1002/2013JD021430>, 2014.

746 Hong, S.-Y., Dudhia, J., and Chen, S.-H.: A Revised Approach to Ice Microphysical
747 Processes for the Bulk Parameterization of Clouds and Precipitation, *Monthly Weather*
748 *Review*, 132, 103-120,
749 [https://doi.org/10.1175/1520-0493\(2004\)132<0103:ARATIM>2.0.CO;2](https://doi.org/10.1175/1520-0493(2004)132<0103:ARATIM>2.0.CO;2), 2004.

750 Hu, G., Lu, M.-H., Reynolds, D., Wang, H.-K., Chen, X., Liu, W.-C., Zhu, F., Wu, X.-W., Xia,
751 F., Xie, M.-C., Cheng, X.-N., Lim, K.-S., Zhai, B.-P., and Chapman, J.: Long-term
752 seasonal forecasting of a major migrant insect pest: the brown planthopper in the Lower
753 Yangtze River Valley, *J. Pest Sci.*, 92, <https://doi.org/10.1007/s10340-018-1022-9>, 2019.

754 Janjić, Z. I.: The step-mountain eta coordinate model: further developments of the convection,
755 viscous sublayer, and turbulence closure schemes, *Monthly Weather Review*, 122,
756 927-945, [https://doi.org/10.1175/1520-0493\(1994\)122<0927:TSMECM>2.0.CO;2](https://doi.org/10.1175/1520-0493(1994)122<0927:TSMECM>2.0.CO;2), 1994.

757 Janjić, Z. I.: Nonsingular implementation of the Mellor-Yamada Level 2.5 Scheme in the NCEP
758 Meso model. NCEP Office Note No. 437, 61 pp., 2002.

759 Jiménez, P. A., Dudhia, J., González-Rouco, J. F., Navarro, J., Montávez, J. P., and
760 García-Bustamante, E.: A Revised Scheme for the WRF Surface Layer Formulation,
761 *Monthly Weather Review*, 140, 898-918, <https://doi.org/10.1175/MWR-D-11-00056.1>,
762 2012.

763 Kain, J. S.: The Kain–Fritsch Convective Parameterization: An Update, *Journal of Applied*
764 *Meteorology*, 43, 170-181,
765 [https://doi.org/10.1175/1520-0450\(2004\)043<0170:TKCPAU>2.0.CO;2](https://doi.org/10.1175/1520-0450(2004)043<0170:TKCPAU>2.0.CO;2), 2004.

766 Li, H., Yin, J., and Kumjian, M.: ZDR Backwards Arc: Evidence of Multi-Directional Size
767 Sorting in the Storm Producing 201.9 mm Hourly Rainfall, *Geophys. Res. Lett.*, 51,
768 e2024GL109192, <https://doi.org/10.1029/2024GL109192>, 2024.

769 Li, M., Sun, J., Li, F., Wu, C., Xia, R., Bao, X., Yin, J., and Liang, X.: Precipitation Evolution
770 from Plain to Mountains during the July 2023 Extreme Heavy Rainfall Event in North
771 China, *Journal of Meteorological Research*, 38, 635-651, 10.1007/s13351-024-3182-2,
772 2024.

773 Lin, Y.-H. and Wu, C.-C.: Remote Rainfall of Typhoon Khanun (2017): Monsoon Mode and
774 Topographic Mode, *Monthly Weather Review*, 149, 733-752,
775 <https://doi.org/10.1175/MWR-D-20-0037.1>, 2021.

776 Mao, J., Ping, F., Yin, L., and Qiu, X.: A Study of Cloud Microphysical Processes Associated
777 With Torrential Rainfall Event Over Beijing, *Journal of Geophysical Research:*
778 *Atmospheres*, 123, 8768-8791, <https://doi.org/10.1029/2018JD028490>, 2018.

779 Meng, Z., Zhang, F., Luo, D., Tan, Z., Fang, J., Sun, J., Shen, X., Zhang, Y., Wang, S., Han, W.,
780 Zhao, K., Zhu, L., Hu, Y., Xue, H., Ma, Y., Zhang, L., Nie, J., Zhou, R., Li, S., Liu, H., and
781 Zhu, Y.: Review of Chinese atmospheric science research over the past 70 years: Synoptic
782 meteorology, *Science China Earth Sciences*, 62, 1946-1991,
783 <https://doi.org/10.1007/s11430-019-9534-6>, 2019.

784 Mlawer, E. J., Taubman, S. J., Brown, P. D., Iacono, M. J., and Clough, S. A.: Radiative transfer
785 for inhomogeneous atmospheres: RRTM, a validated correlated-k model for the longwave,
786 *Journal of Geophysical Research: Atmospheres*, 102, 16663-16682,
787 <https://doi.org/10.1029/97JD00237>, 1997.

788 Tomas, P., Pieter, G., and Ivan, T.: Vertical wind shear and convective storms,
789 <https://doi.org/10.21957/z0b3t5mrv>, 2021.

790 Rao, C., Chen, G., and Ran, L.: Effects of Typhoon In-Fa (2021) and the Western Pacific

791 Subtropical High on an Extreme Heavy Rainfall Event in Central China, *Journal of*
792 *Geophysical Research: Atmospheres*, 128, e2022JD037924,
793 <https://doi.org/10.1029/2022JD037924>, 2023.

794 Rotunno, R., Klemp, J., and Weisman, M.: A Theory for Strong, Long-Lived Squall Lines,
795 *Journal of The Atmospheric Sciences - J ATMOS SCI*, 45, 463-485,
796 [https://doi.org/10.1175/1520-0469\(1988\)045<0463:ATFSLL>2.0.CO;2](https://doi.org/10.1175/1520-0469(1988)045<0463:ATFSLL>2.0.CO;2), 1988.

797 Schumacher, R. S. and Rasmussen, K. L.: The formation, character and changing nature of
798 mesoscale convective systems, *Nature Reviews Earth & Environment*, 1, 300-314,
799 [10.1038/s43017-020-0057-7](https://doi.org/10.1038/s43017-020-0057-7), 2020.

800 Stauffer, D. R., Seaman, N. L., and Binkowski, F. S.: Use of Four-Dimensional Data
801 Assimilation in a Limited-Area Mesoscale Model Part II: Effects of Data Assimilation
802 within the Planetary Boundary Layer, *Monthly Weather Review*, 119, 734-754,
803 [https://doi.org/10.1175/1520-0493\(1991\)119<0734:UOFDDA>2.0.CO;2](https://doi.org/10.1175/1520-0493(1991)119<0734:UOFDDA>2.0.CO;2), 1991.

804 Sun, J., Qi, L., and Zhao, S.: A study on mesoscale convective systems of the severe heavy
805 rainfall in north China by “9608” typhoon, *Acta Meteorologica Sinica*, 64, 57-71,
806 [10.11676/qxxb2006.006](https://doi.org/10.11676/qxxb2006.006), 2006.

807 Sun, Y., Zhong, Z., Yi, L., Li, T., Chen, M., Wan, H., Wang, Y., and Zhong, K.: Dependence of
808 the relationship between the tropical cyclone track and western Pacific subtropical high
809 intensity on initial storm size: A numerical investigation, *Journal of Geophysical Research:*
810 *Atmospheres*, 120, 11,451-411,467, <https://doi.org/10.1002/2015JD023716>, 2015.

811 Tewari, M., Chen, F., Wang, W., Dudhia, J., LeMone, M. A., Mitchell, K., Ek, M., Gayno, G.,
812 Wegiel, J., and Cuenca, R. H.: Implementation and verification of the unified NOAA land
813 surface model in the WRF model. 20th conference on weather analysis and
814 forecasting/16th conference on numerical weather prediction, pp. 11-15., 2004.

815 Thompson, G., Field, P. R., Rasmussen, R. M., and Hall, W. D.: Explicit Forecasts of Winter
816 Precipitation Using an Improved Bulk Microphysics Scheme. Part II: Implementation of a
817 New Snow Parameterization, *Monthly Weather Review*, 136, 5095-5115,
818 <https://doi.org/10.1175/2008MWR2387.1>, 2008.

819 Wang, Y., Wang, Y., and Fudeyasu, H.: The Role of Typhoon Songda (2004) in Producing
820 Distantly Located Heavy Rainfall in Japan, *Monthly Weather Review*, 137, 3699-3716,
821 <https://doi.org/10.1175/2009MWR2933.1>, 2009.

822 Xia, R., Ruan, Y., Sun, J., Liang, X., Li, F., Wu, C., Li, J., Yin, J., Bao, X., Li, M., and Gao, X.:
823 Distinct Mechanisms Governing Two Types of Extreme Hourly Rainfall Rates in the
824 Mountain Foothills of North China During the Passage of a Typhoon Remnant Vortex
825 from July 30 to August 1, 2023, *Advances in Atmospheric Sciences*,
826 <https://doi.org/10.1007/s00376-024-4064-3>, 2025.

827 Xia, R. and Zhang, D.-L.: An Observational Analysis of Three Extreme Rainfall Episodes of
828 19–20 July 2016 along the Taihang Mountains in North China, *Monthly Weather Review*,
829 147, 4199-4220, <https://doi.org/10.1175/MWR-D-18-0402.1>, 2019.

830 Xu, H. and Li, X.: Torrential rainfall processes associated with a landfall of Typhoon Fitow
831 (2013): A three-dimensional WRF modeling study, *Journal of Geophysical Research:*
832 *Atmospheres*, 122, 6004-6024, <https://doi.org/10.1002/2016JD026395>, 2017.

833 Xu, H., Zhang, D., and Li, X.: The Impacts of Microphysics and Terminal Velocities of
834 Graupel/Hail on the Rainfall of Typhoon Fitow (2013) as Seen From the WRF Model
835 Simulations With Several Microphysics Schemes, *Journal of Geophysical Research:*
836 *Atmospheres*, 126, e2020JD033940, <https://doi.org/10.1029/2020JD033940>, 2021.

837 Xu, H., Li, X., Yin, J., and Zhang, D.: Predecessor Rain Events in the Yangtze River Delta
838 Region Associated with South China Sea and Northwest Pacific Ocean (SCS-WNPO)
839 Tropical Cyclones, *Advances in Atmospheric Sciences*, 40, 1021-1042,
840 <https://doi.org/10.1007/s00376-022-2069-3>, 2023a.

841 Xu, H., Zhao, D., Yin, J., Duan, Y., Gao, W., Li, Y., and Zhou, L.: Indirect Effects of Binary
842 Typhoons on an Extreme Rainfall Event in Henan Province, China From 19 to 21 July
843 2021. 3. Sensitivities to Microphysics Schemes, *Journal of Geophysical Research:*
844 *Atmospheres*, 128, e2022JD037936, <https://doi.org/10.1029/2022JD037936>, 2023b.

845 Yang, L., Liu, M., Smith, J. A., and Tian, F.: Typhoon Nina and the August 1975 Flood over
846 Central China, *Journal of Hydrometeorology*, 18, 451-472,

847 <https://doi.org/10.1175/JHM-D-16-0152.1>, 2017.

848 Yin, J., Liang, X., Wang, H., and Xue, H.: Representation of the autoconversion from cloud to
849 rain using a weighted ensemble approach: a case study using WRF v4.1.3, *Geosci. Model*
850 *Dev.*, 15, 771-786, <https://doi.org/10.5194/gmd-15-771-2022>, 2022a.

851 Yin, J., Zhang, D.-L., Luo, Y., and Ma, R.: On the Extreme Rainfall Event of 7 May 2017 Over
852 the Coastal City of Guangzhou. Part I: Impacts of Urbanization and Orography, *Monthly*
853 *Weather Review*, 148, 955-979, <https://doi.org/10.1175/MWR-D-19-0212.1>, 2020.

854 Yin, J., Gu, H., Yu, M., Bao, X., Xie, Y., and Liang, X.: Synergetic Roles of Dynamic and Cloud
855 Microphysical Processes in Extreme Short-Term Rainfall: A Case Study, *Quarterly*
856 *Journal of the Royal Meteorological Society*, 148, 3660- 3676,
857 <https://doi.org/10.1002/qj.4380>, 2022b.

858 Yin, J., Wang, D., Liang, Z., Liu, C., Zhai, G., and Wang, H.: Numerical Study of the Role of
859 Microphysical Latent Heating and Surface Heat Fluxes in a Severe Precipitation Event in
860 the Warm Sector over Southern China, *Asia-Pacific Journal of Atmospheric Sciences*, 54,
861 77-90, <https://doi.org/10.1007/s13143-017-0061-0>, 2018.

862 Yin, J., Gu, H., Liang, X., Yu, M., Sun, J., Xie, Y., Li, F., and Wu, C.: A Possible Dynamic
863 Mechanism for Rapid Production of the Extreme Hourly Rainfall in Zhengzhou City on 20
864 July 2021, *Journal of Meteorological Research*, 36, 6-25,
865 <https://doi.org/10.1007/s13351-022-1166-7>, 2022c.